Colloids and Surfaces A: Physicochemical and Engineering Aspects 721 (2025) 137215

Contents lists available at ScienceDirect

Colloids and Surfaces A: Physicochemical and Engineering Aspects

journal homepage: www.elsevier.com/locate/colsurfa

# Construction of hierarchical S-scheme $MgIn_2S_4/CeO_2$ heterojunction for boosted photocatalytic oxidation of tetracycline and reduction of Cr(VI)

Damilola Caleb Akintayo [a], Tunde Lewis Yusuf [b,*], Nonhlangabezo Mabuba [a,c,**]

[a] Department of Chemical Sciences, Faculty of Science, University of Johannesburg, Doornfontein Campus, Johannesburg 2028, South Africa
[b] Department of Chemistry, Faculty of Natural and Agricultural Sciences, University of Pretoria, Private Bag X20, Hatfield, Pretoria 0028, South Africa
[c] Center for Nanomaterials Science Research, Faculty of Science, University of Johannesburg, Doornfontein Campus, Johannesburg 2028, South Africa

## GRAPHICAL ABSTRACT

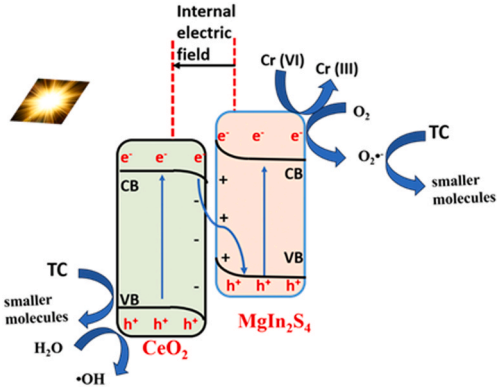


## ARTICLE INFO

*Keywords:*
Photoreduction
Photooxidation
S-scheme, $MgIn_2S_4$
$CeO_2$

## ABSTRACT

This study explores the photocatalytic performance of a hierarchical $MgIn_2S_4/CeO_2$ S-scheme heterojunction, emphasizing its structural, morphological, and electronic features. The heterojunction was synthesized *in situ* by integrating a porous $MgIn_2S_4$ framework with $CeO_2$ nanorods. Comprehensive characterization techniques such as XRD, XPS, FE-SEM, TEM, and BET confirm the heterojunction's formation and reveal its enhanced surface area, hierarchical porosity, and interfacial electronic interactions. Furthermore, the optical and photoelectrochemical properties were investigated through UV-Vis DRS, photoluminescence spectroscopy, photocurrent response, and EIS, thus demonstrating enhanced visible light absorption, reduced charge recombination, and efficient charge transfer. The photocatalytic tests show that $MgIn_2S_4/CeO_2$ has a degradation efficiency of 86 % for the photooxidation of tetracycline and 96 % for the photoreduction of Cr(VI) after 120 min. The enhanced properties can be attributed to the S-scheme heterostructure, which facilitates better charge transfer and separation and preserves the high redox potential photogenerated carriers for photocatalytic reactions. The degradation products of tetracycline were confirmed using HPLC–MS analysis. This work provided a systematic

* Corresponding author.
** Corresponding author at: Department of Chemical Sciences, Faculty of Science, University of Johannesburg, Doornfontein Campus, Johannesburg 2028, South Africa.
*E-mail addresses:* yusuf.tl@up.ac.za (T.L. Yusuf), nmabuba@uj.ac.za (N. Mabuba).

https://doi.org/10.1016/j.colsurfa.2025.137215
Received 25 March 2025; Received in revised form 23 April 2025; Accepted 13 May 2025
Available online 13 May 2025

approach to designing advanced photocatalysts with promising applications in environmental remediation, and the findings contribute to the development of sustainable technologies for wastewater treatment.

## 1. Introduction

Water pollution, contaminating water bodies with harmful substances, poses serious risks to human health and ecosystems. Polluted water leads to waterborne diseases, while toxic chemicals like pharmaceuticals and heavy metals can cause chronic illnesses and neurological damage. Economically, water pollution reduces agricultural productivity and access to clean water and sanitation [1–3]. Examples of these pollutants include tetracycline (TC) and Chromium(VI). Tetracycline, a widely used antibiotic, is a significant water pollutant due to its persistence in aquatic environments and resistance to conventional water treatment processes. It enters water systems through pharmaceutical manufacturing waste, agricultural runoff, and improper disposal of medications [4,5]. Tetracycline residues can disrupt aquatic ecosystems, harm beneficial microorganisms, and contribute to the development of antibiotic-resistant bacteria, posing risks to both environmental and human health [6,7]. On the other hand, Chromium(VI) is a toxic heavy metal commonly found in industrial waste from electroplating, leather tanning, and stainless-steel production processes. It is highly soluble and mobile in water, making it a significant environmental pollutant [8]. Chromium(VI) poses serious health risks, including carcinogenicity, mutagenicity, and damage to the respiratory, digestive, and immune systems when ingested or inhaled. Its presence in water bodies can also harm aquatic ecosystems by disrupting biological processes [9,10]. Thus, the growing challenge of these pollutants in water systems highlights the pressing demand for advanced, efficient, and environmentally sustainable remediation strategies.

In recent years, photocatalysis has emerged as a promising green technology for water purification, leveraging semiconductor materials to harness light energy for the degradation of organic pollutants and the reduction of heavy metals [11–13]. Photocatalysis offers several advantages over conventional water treatment technologies, making it an effective and sustainable option for removing pollutants [14,15]. Unlike adsorption or chemical treatments, photocatalysis completely degrades contaminants into harmless byproducts like water and carbon dioxide rather than transferring pollutants to another phase or generating secondary waste [16]. The process operates under mild conditions, requiring only a light source and a photocatalyst, making it energy-efficient and cost-effective [17]. Additionally, it avoids harsh chemicals, making it environmentally friendly and suitable for decentralized water treatment applications.

Moreover, photocatalysis is a type of advanced oxidation process (AOP) that involves using photocatalysts and light energy [18]. When a photocatalyst is exposed to light with energy equal to or greater than the photocatalyst's bandgap, electron-hole pairs are generated. The photoexcited electrons in the conduction band enable photoreduction, reducing pollutants such as Cr(VI) to the less toxic Cr(III). Concurrently, the holes in the valence band drive photooxidation, oxidizing water or other species to produce highly reactive oxygen species (ROS), such as hydroxyl radicals, which degrade organic pollutants [19]. This dual mechanism effectively transforms organic and inorganic contaminants into safer or less harmful substances, making photocatalysis a robust and sustainable AOP for water treatment. However, the challenges associated with this process include the inability of some single photocatalysts to harness visible light energy, the rapid recombination of photoexcited charge carriers, and the failure to target various pollutants [20]. Some photocatalysts are effective for degrading organic pollutants but perform poorly in reducing heavy metals, and vice versa. These limitations can be addressed by employing strategies such as heterojunction formation.

Amongst several reported heterojunctions, developing the S-scheme heterojunction has emerged as a promising strategy to overcome the limitations of the single photocatalyst in water treatment [21]. An S-scheme, also known as the step-scheme heterojunction, is formed from an oxidation photocatalyst and a reduction photocatalyst with complementary band energies aligned in a staggered structure to facilitate charge mobility and separation [22]. Unlike the traditional heterojunctions, the S-scheme mechanism preserves the strong redox potentials of the individual semiconductor and allows the charge carriers with lower oxidation and reduction potential to recombine [23,24]. Various S-scheme heterojunction photocatalysts such as $Ag_2CO_3$/-$Bi_4O_5I_2$/g-$C_3N_4$[25], $BiOCl/CuBi_2O_4$ [26], g-$C_3N_4/TiO_2$ [27], $WO_3/CeO_2$ [28], $FeOOH/MgIn_2S_4$ [29], and so on have been reported for the photocatalytic degradation of pharmaceutical compounds in water. However, the photoreduction efficiency of these heterojunctions was not tested.

In this work, we constructed an S-scheme heterojunction from the combination of magnesium Indium sulfide ($MgIn_2S_4$) and cerium oxide ($CeO_2$) for the photooxidation of tetracycline and also for the photoreduction of Cr(VI). $CeO_2$ is a widely studied photocatalyst due to its unique optical, surface, and electronic properties. It reversibly converts between two oxidation states, $Ce^{+3}$ and $Ce^{4+,}$ enhancing its redox activity [30]. In addition, it is chemically stable and environmentally friendly [31]. Despite its photocatalytic activity, $CeO_2$ has drawbacks such as the agglomeration of its nanoparticles, weak absorption of visible light, and fast recombination rate of photoexcited charge carriers [30,32,33]. On the other hand, $MgIn_2S_4$ is a chalcogenide semiconductor with a layered structure and a narrow bandgap that can efficiently utilize visible light. It is stable, and its 2D morphology can facilitate charge carrier mobility [34,35]. Nevertheless, its band edge positions and band gap energy might limit its photooxidation efficiency in photocatalytic reactions and make it suffer from charge carrier recombination. Therefore, utilizing the unique properties of $MgIn_2S_4$ and $CeO_2$ is expected to enhance the electronic and photocatalytic properties for the photooxidation and photoreduction of organic compounds and heavy metals.

Thus, this study aims to explore and understand the strategy involved in constructing an S-scheme heterojunction that can efficiently oxidize and reduce pollutants. To our understanding, this is the first report to comprehensively construct, characterize, and apply $MgIn_2S_4$/$CeO_2$ S-scheme heterojunction. Hence, this study provides insights into the design of advanced photocatalysts for the dual-purpose treatment of organic pollutants and heavy metals. The findings in this work contribute to the broader understanding of the dynamics of charge carriers in semiconductor heterojunction for photocatalysis.

## 2. Experimental section

### 2.1. Chemicals

Cerium nitrate hexahydrate ($Ce(NO_3)_3{\cdot}6\ H_2O$), sodium hydroxide (NaOH), L-cysteine, magnesium nitrate hexahydrate ($Mg(NO_3)_2{\cdot}6\ H_2O$), deionized water, indium chloride ($InCl_3$), ethanol, potassium hexacyanoferrate (II) ($K_4[Fe(CN)_6]$), polyvinylidene fluoride (PVDF), ethylenediaminetetraacetic acid disodium salt ($Na_2EDTA$), silver nitrate ($AgNO_3$), p-Benzoquinone (BQ), isopropanol (IPA), Tetracycline (TC), potassium chromate ($K_2Cr_2O_7$), potassium hexacyanoferrate (III) ($K_3[Fe(CN)_6]$), and N-methyl-2-pyrrolidone (NMP) were used for this study and purchased from Sigma-Aldrich (South Africa)

### 2.2. Photocatalysts synthesis

#### 2.2.1. Synthesis of cerium oxide ($CeO_2$) nanorods

Cerium oxide ($CeO_2$) nanorods were synthesized using a simple hydrothermal method [32]. In a typical synthesis, cerium nitrate hexahydrate ($Ce(NO_3)_3{\cdot}6\ H_2O$, 3.48 g) was gradually added to a stirred sodium hydroxide (NaOH, 9.8 g) solution at room temperature. The mixture was stirred for 30 minutes and subsequently transferred to a sealed autoclave, where it was subjected to thermal treatment at 100 °C for 24 hours. After cooling to room temperature, the resulting product was recovered by filtration, thoroughly washed with deionized water and absolute ethanol, and dried at 80 °C overnight; a yellow powder of $CeO_2$ was obtained.

#### 2.2.2. Synthesis of $MgIn_2S_4$

$Mg(NO)_2\ {\cdot}6\ H_2O$ (0.2 mmol), 0.4 mmol of $InCl_3$, and 0.9 mmol of L-cysteine were weighed and added to a beaker. The resulting solution was continuously stirred for 1 hr, and then the mixture was transferred to a Teflon-lined autoclave and heated in a furnace at 180°C for 24 hr. The precipitate formed was collected by centrifugation and washed thrice with deionized water and ethanol. The precipitate was dried for 8 hr at 70°C to obtain a pure $MgIn_2S_4$.

#### 2.2.3. Synthesis of $MgIn_2S_4/CeO_2$

The synthesized $CeO_2$ (1 mmol) was dispersed in 60 mL of deionized water through ultrasonication for 15 minutes, followed by the synthesis of $MgIn_2S_4$, as reported in Section 2.2.2. Briefly, to the dispersed solution $CeO_2$, 0.2 mmol of $Mg(NO_3)_2{\cdot}6\ H_2O$, 0.4 mmol of $InCl_3$, and 0.9 mmol of L-cysteine were added, followed by continuous stirring for 1 hour. The resulting mixture was transferred to a Teflon-lined autoclave and heated in a furnace at 180°C for 24 hours. The product formed was collected by centrifugation, washed three times each with deionized water and ethanol, and dried overnight in an oven at 70°C.

### 2.3. Characterization

#### 2.3.1. Characterization and instruments used

X-ray diffraction (XRD) analysis was conducted on a D8 Advance diffractometer using Cu Kα radiation (λ = 154.18 pm) in Bragg–-Brentano mode. The morphology of the samples was examined through a field-emission scanning electron microscope (FE-SEM, JEOL JSM-7500F, Japan). Electronic absorption measurements were carried out with a Cary 60 UV–vis spectrophotometer (Agilent Technologies, Malaysia). X-ray photoelectron spectroscopy (XPS) data were collected using a Kratos Axis supra+ spectrometer equipped with monochromatic Al Kα radiation (hv = 1486.6 eV) and operating at 150 W. Electrochemical impedance spectroscopy (EIS), Mott-Schottky, and photocurrent response analyses were performed using an Autolab Potentiostat (PGSTAT204, Netherlands. The setup comprised a platinum wire as the counter electrode, an Ag/AgCl electrode (3.0 M KCl) as the reference electrode, and a working electrode prepared by coating a fluorine-doped tin oxide (FTO) substrate (1.5 cm × 1.5 cm) with 30 mg of the synthesized material. A binder mixture of 5 wt% PVDF and 100 μL NMP was used for the electrode preparation [36]. For EIS analysis, measurements were conducted in a solution containing 5 mM $[Fe(CN)_6]^{3/4-}$ dissolved in 0.1 M KCl at an applied potential of + 0.25 V without light, across a frequency range from 100 kHz to 0.1 Hz. Impedance data were analyzed using a Randle circuit model. Mott-Schottky measurements were carried out under dark conditions with the 5 mM $[Fe(CN)_6]^{3/4-}$ in 0.1 M KCl electrolyte solution. The photocurrent response measurements were conducted in 0.1 M $Na_2SO_4$ applying a bias potential of 1.5 V with reference to the Ag/AgCl electrode. Brunauer–Emmett–Teller (BET) analysis was employed to determine the surface area, while the Barrett-Joyner-Halenda (BJH) model was utilized to calculate the porosity of the samples at liquid nitrogen temperature. Prior to analysis, the samples were degassed for 8 hours at 80°C using an ASAP 2020 instrument (Micromeritics Corporation, Version 4.00). The degradation pathway for photoelectrochemical (PEC) degradation was analyzed using ultra-performance liquid chromatography coupled with mass spectrometry (UPLC-MS) (WATERS, USA). Photoluminescence (PL) spectroscopy (F-186 2710, HITACHI, Japan) was employed to investigate the recombination rate of photogenerated charge carriers

### 2.4. Photocatalytic tests

A Xenon solar lamp (100 W) was utilized as the light source for investigating the photooxidation of tetracycline (TC) and the photoreduction of Cr (VI). The lamp was positioned at a distance of 10 cm from the solution's surface. In the experiments, 50 mL of TC solution (10 mg/L, pH 7) and 50 mL of Cr (VI) solution (10 mg/L, pH 5.8) were prepared. 40 mg of the catalyst was dispersed in each pollutant solution and stirred under dark conditions for 20 minutes to allow adsorption-desorption equilibrium. Afterward, the lamp was switched on, and at regular intervals, 3 mL of the degraded sample was withdrawn from the solution, followed by centrifugation at 7000 rpm for 10 minutes to remove the catalyst effectively. The TC concentration was monitored using a spectrophotometer, and the Cr(VI) concentration was quantified using the 1,5-diphenylcarbazide (DPC) method, ensuring accurate analysis of its reduction.

The percentage extent of degradation was calculated using Eq. 1

$$\%Degradation\ efficiency = \left(1 - \frac{C_t}{C_o}\right) * 100 \quad (1)$$

Where $C_t$ = Concentration of TC or Cr(VI) in mg/L after degradation and $C_o$ = Initial concentration of TC or Cr(VI) in mg/L before degradation

### 2.5. The determination of reactive species

The primary reactive species involved in the degradation process were identified through free radical quenching experiments. Various scavengers' concentrations were employed to trap specific reactive species: hydroxyl radicals were trapped using 0.2 mmol/L isopropanol (IPA), superoxide radicals were scavenged with 0.2 mmol/L p-benzoquinone, photogenerated holes were captured using 0.2 mmol/L sodium ethylenediaminetetraacetate ($Na_2EDTA$), and photogenerated electrons were trapped using 0.2 mmol/L silver nitrate ($AgNO_3$).

## 3. Results and discussions

### 3.1. Structure, composition, and morphology studies

The X-ray diffraction (XRD) analysis was used to investigate the crystalline phases of the as-synthesized $CeO_2$, $MgIn_2S_4$, and $MgIn_2S_4/CeO_2$ composite. As shown in Fig. 1a, the diffraction pattern of the pristine $CeO_2$ exhibits the characteristic peaks at 2θ values of 28.3°, 32.8°, 47.3°, 56.2°, 69.2°, 76.5°, 79.1°, and 88.4°, corresponding respectively to the (111), (200), (220), (311), (222), (400), (331), and (420) hkl crystal planes of the cubic $CeO_2$ with the JCPDS no. 01–080–5549 [33]. Similarly, the diffraction pattern of $MgIn_2S_4$ shows distinct peaks at 23.4°, 27.5°, 33.1°, 43.5°, and 47.7° that are well indexed to the (220), (311), (400), (333) and (440) planes respectively, of the cubic phase $MgIn_2S_4$ with the JCPDS no. of 04–007–9835 [37]. In the diffraction pattern of the $MgIn_2S_4/CeO_2$ composite, the significant characteristics peak of $CeO_2$ and $MgIn_2S_4$ were observed at 23.2° 27.3°, 28.1°, 32.9°, 43.5°, 47.6°, and 56.1°, thus confirming the formation of the composite. The doublet peak observed can be due to the overlap of peaks at 27.5° (311) of $MgIn_2S_4$ and 28.3° (111) of $CeO_2$, suggesting the interaction between $CeO_2$ and $MgIn_2S_4$ at the interface. Otherwise, no significant shift was observed in the peaks of $CeO_2$ and $MgIn_2S_4$ in the composite, suggesting insignificant distortion in their crystal lattice and successful synthesis of a heterostructure.

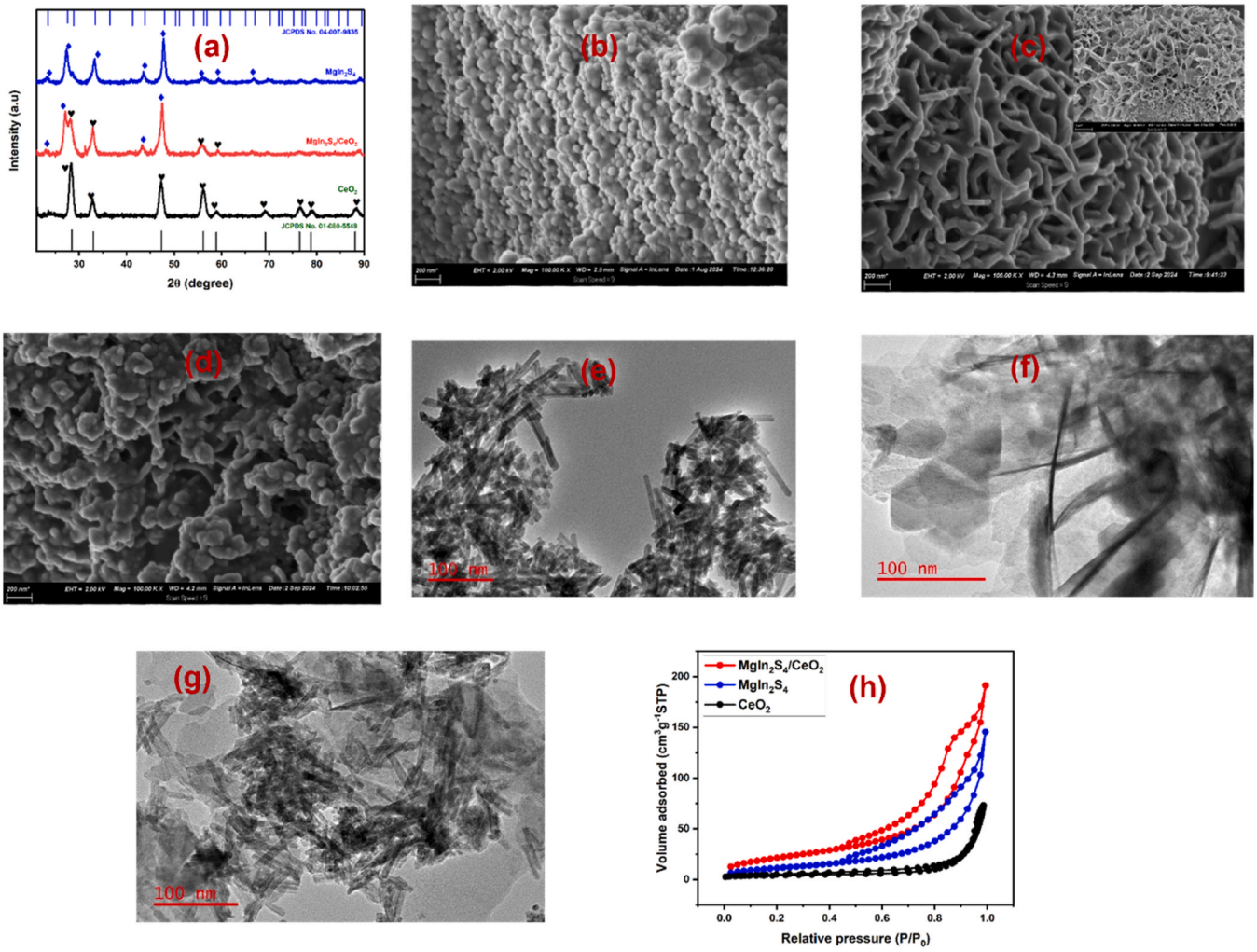


**Fig. 1.** (a) XRD spectra of $CeO_2$, $MgIn_2S_4$, & $MgIn_2S_4/CeO_2$. FESEM micrograph of (b) $CeO_2$, (c) $MgIn_2S_4$, (d) $MgIn_2S_4/CeO_2$. TEM micrograph of (e) $CeO_2$, (f) $MgIn_2S_4$, (g) $MgIn_2S_4/CeO_2$. (h) $N_2$ adsorption-desorption spectra of $CeO_2$, $MgIn_2S_4$, & $MgIn_2S_4/CeO_2$.

The FESEM micrograph of $CeO_2$ (Fig. 1b) reveals that $CeO_2$ nanoparticles possess relatively small smoothness. And uniformly distributed spherical particles in a cluster-like arrangement. This morphology supports efficient light absorption and charge mobility for effective photocatalytic activity [38]. In Fig. 1c, the FESEM micrograph of $MgIn_2S_4$ displays a network-like structure characterized by an interconnected framework of nanoflower. Also, it shows a porous and hierarchical structure with empty spaces between the individual particles. Moreover, high porosity enhances surface area and increases active sites for photocatalytic reactions [39]. The FESEM micrograph of $MgIn_2S_4/CeO_2$ composite (Fig. 1d) also reveals a well-integrated structure of $CeO_2$ and $MgIn_2S_4$. The heterojunction formation is evident from the close interaction of the two phases where the interconnected nanoflower-like structure of MgIn2S4 acts as a matrix, with $CeO_2$ stacked nanoparticles embedded within the porous framework. Overall, the interaction promotes efficient charge mobility and separation. The TEM analysis of the $MgIn_2S_4/CeO_2$ heterojunction further confirms its unique structural attributes. The $MgIn_2S_4$ component is observed as fine nanosheets forming nanoflower-like morphologies, consistent with its high surface area and porous nature. On the other hand, $CeO_2$ appears as non-distinct, irregular nanorods, contributing to its characteristic structural properties. In the composite, the TEM micrographs distinctly reveal the integration of these two phases. The $MgIn_2S_4$ nanoflowers serve as a scaffold, providing a hierarchical and porous framework, while the $CeO_2$ nanorods are well-dispersed and embedded within the matrix. Combining these morphologies results in a synergistic effect, where the intimate contact and distribution of $CeO_2$ within the $MgIn_2S_4$ framework facilitate efficient interfacial interactions.

These structural characteristics confirm the successful synthesis of the heterojunction and highlight the composite morphology's role in enhancing charge separation and mobility. The hierarchical arrangement allows for better light absorption and greater exposure to active sites, further supporting its superior photocatalytic performance. In addition, the surface area and porosity of the materials were investigated through nitrogen adsorption-desorption measurements. As displayed in Fig. 1e, the pristine photocatalyst and composite exhibited the characteristics of a type IV isotherm, indicating mesoporous structures characterized by large pore volumes and high surface areas. Amongst the materials, the $MgIn_2S_4/CeO_2$ heterojunction demonstrated superior structural properties in terms of surface area compared to $CeO_2$ and $MgIn_2S_4$, as summarized in Table 1. Notably, the $MgIn_2S_4/CeO_2$ heterojunction exhibited the highest specific surface area of 73.23 $m^2/g$.

**Table 1**
BET surface area and pore volume of the photocatalysts.

| Photocatalysts | BET Surface area($m^2/g$) | Pore volume ($cm^3/g$) |
|---|---|---|
| $CeO_2$ | 45.28 | 0.292 |
| $MgIn_2S_4$ | 56.76 | 0.226 |
| $MgIn_2S_4/CeO_2$ | 73.23 | 0.330 |

Interestingly, $CeO_2$ has the highest pore volume but the lowest surface area, which could correspond to its porosity being dominated by larger mesopores. On the other hand, $MgIn_2S_4$ has a denser layered structure, which reduces its pore volume.

Furthermore, X-ray photoelectron spectroscopy (XPS)was employed to investigate the elemental composition of the materials. The XPS spectra provide an understanding of the bonding environment and electronic interaction between $CeO_2$ and $MgIn_2S_4$. The high-resolution XPS spectra of each element present in the photocatalyst were analyzed. Fig. 2a shows the Ce 3d spectra of both the pristine $CeO_2$ and $MgIn_2S_4/CeO_2$; the spectra are characterized by two sets of spin-orbit doublets, which correspond to 3d5/2 and 3d3/2 that further split into satellite peaks, due to the presence of different oxidation states of cerium ($Ce^{3+}$ and $Ce^{4+}$) [40]. For the pristine $CeO_2$, the peaks at position 883.3 eV and 899.1 eV represent the Ce 3d5/2 and Ce 3d3/2 orbitals, respectively, hence confirming the predominance of the $Ce^{4+}$ state in $CeO_2$. The minor peaks at 889 eV and 907.7 eV indicate the coexistence of $Ce^{3+}$ states, which contribute to the redox capacity of $CeO_2$. In the $MgIn_2S_4/CeO_2$ composite, a decrease in the binding energy of the peaks associated with the $Ce^{4+}$ state (882.4 eV and 898.4 eV) was observed. Moreover, a noticeable change in the intensity of the peaks related to $Ce^{3+}$ at 889 eV and 907.7 eV was observed, suggesting an increase in the proportion of $Ce^{3+}$ species, which can be attributed to the interfacial charge transfer between $CeO_2$ and $MgIn_2S_4$. For the O 1 s spectra (Fig. 2b), two peaks attributed to lattice oxygen and surface adsorbed oxygen were observed at 529.9 eV and 532.0 eV for $CeO_2$, and 529.5 eV and 531.3 eV for $MgIn_2S_4/CeO_2$ composite, respectively. Again, a shift to a lower binding energy observed suggests a strong interaction between $CeO_2$ and $MgIn_2S_4$ in the composite. Furthermore, the Mg 1 s peak of $MgIn_2S_4$ (Fig. 2c) is observed at a binding energy of 1304.5 eV, while the peak of $MgIn_2S_4/CeO_2$ (Fig. 2d) was observed to shift to a lower binding energy of 1304.2 eV [29,37]. This slight reduction can be attributed to a change in the electronic environment of $Mg^{2+}$ due to heterojunction formation. In addition, the In 3d spectra of $MgIn_2S_4$ and $MgIn_2S_4/CeO_2$ (Fig. 2e) show two well-defined peaks of In $3d_{5/2}$ and In $3d_{3/2}$ states located at 444.5 eV & 451.97 eV and 444.6 eV & 452.1 eV, respectively [29,41]. These peaks confirm the presence of $In^{3+}$ in the indium lattice. Lastly, the S 2p spectra (Fig. 2f) show two peaks at 161.0 eV & 164.0 eV for $MgIn_2S_4$ and 161.3 eV & 164.0 eV, which correspond to S $2p_{3/2}$ and S $2p_{1/2}$ states, respectively. This confirms the presence of $S^{2-}$ in the sulfide lattice. These shifts to higher binding energies in the composite can be attributed to a decrease in electron density around indium and sulfur caused by electron transfer from $MgIn_2S_4$ to $CeO_2$. These results suggest an interfacial interaction between $CeO_2$ and $MgIn_2S_4$, which are essential in forming an S-scheme heterojunction for enhanced photogenerated charge carrier transfer and separation required for boosting the photocatalytic efficiency of the $MgIn_2S_4/CeO_2$ photocatalyst.

### 3.2. Optical studies

The light absorption properties of $CeO_2$, $MgIn_2S_4$, and $MgIn_2S_4/CeO_2$ were analyzed using the UV-Vis DRS spectra (Fig. 3a). The pristine $CeO_2$ possesses a strong absorption edge at approximately 519 nm, while $MgIn_2S_4$ displays absorption that extends into the visible light region, with an absorption edge around 641 nm. For the $MgIn_2S_4/CeO_2$ composite, the absorption spectra show a redshift when compared to $CeO_2$, with an absorption edge of 620 nm, corresponding to a heterojunction formation. Using the UV-Vis DRS data, the band gaps were estimated using Tauc plots; the band gap energies of 1.84 eV and 2.37 eV were observed for $MgIn_2S_4$ and $CeO_2$ (Fig. 3b), respectively. Therefore, the absorption range of $MgIn_2S_4/CeO_2$ confirms its ability to harvest light in the visible region.

Photoluminescence (PL) spectroscopy was used to examine the charge recombination behavior of the photocatalysts. As shown in Fig. 3c, $CeO_2$ has a higher intensity emission peak at around 466 nm, indicating a high recombination rate of photoexcited charge carriers. However, the PL spectrum of $MgIn_2S_4$ was not detected, which is likely

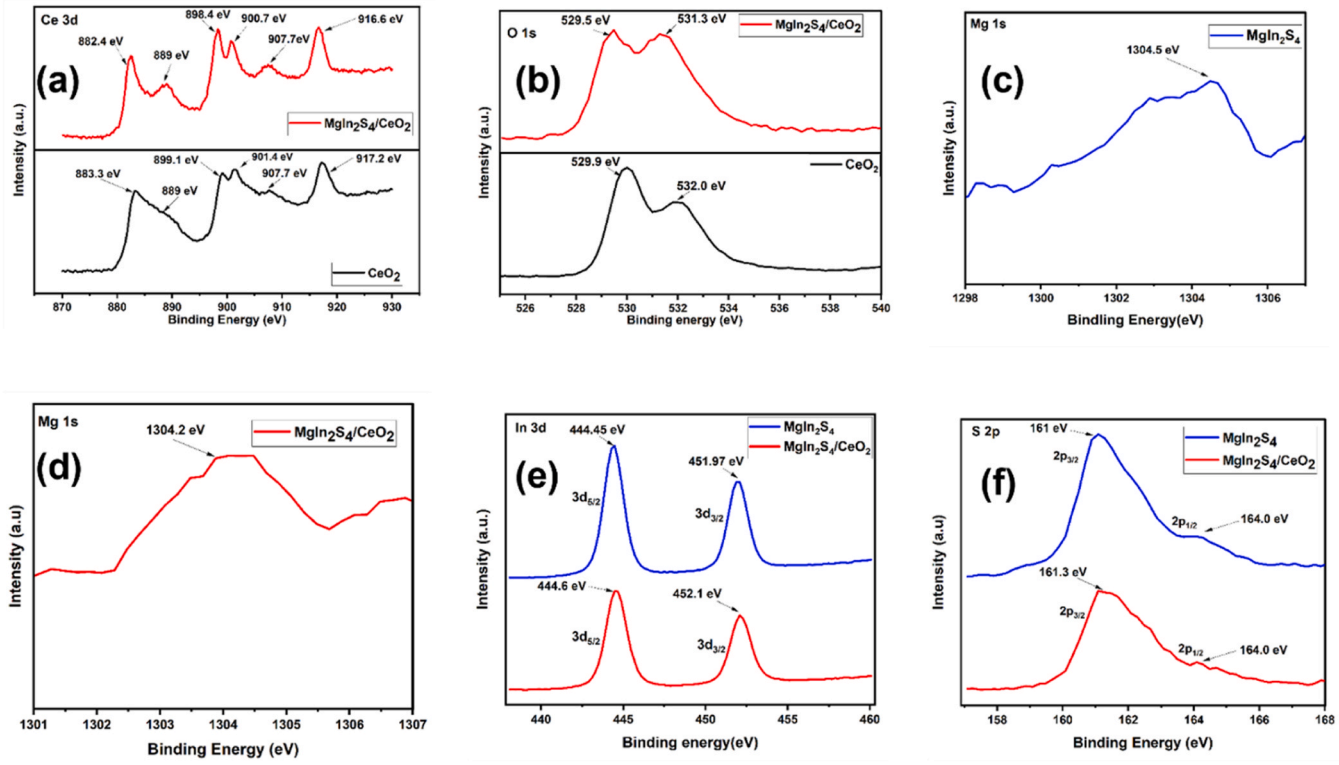


**Fig. 2.** High-resolution XPS spectra of (a) Ce 3d of $CeO_2$ and $MgIn_2S_4/CeO_2$, (b) O 1 s of $CeO_2$ and $MgIn_2S_4/CeO_2$, (c) Mg 1 s of $MgIn_2S_4$, (d) Mg 1 s of $MgIn_2S_4/CeO_2$, (e) In 3d of $MgIn_2S_4$ and $MgIn_2S_4/CeO_2$, (f) S 2p of $MgIn_2S_4$ and $MgIn_2S_4/CeO_2$.

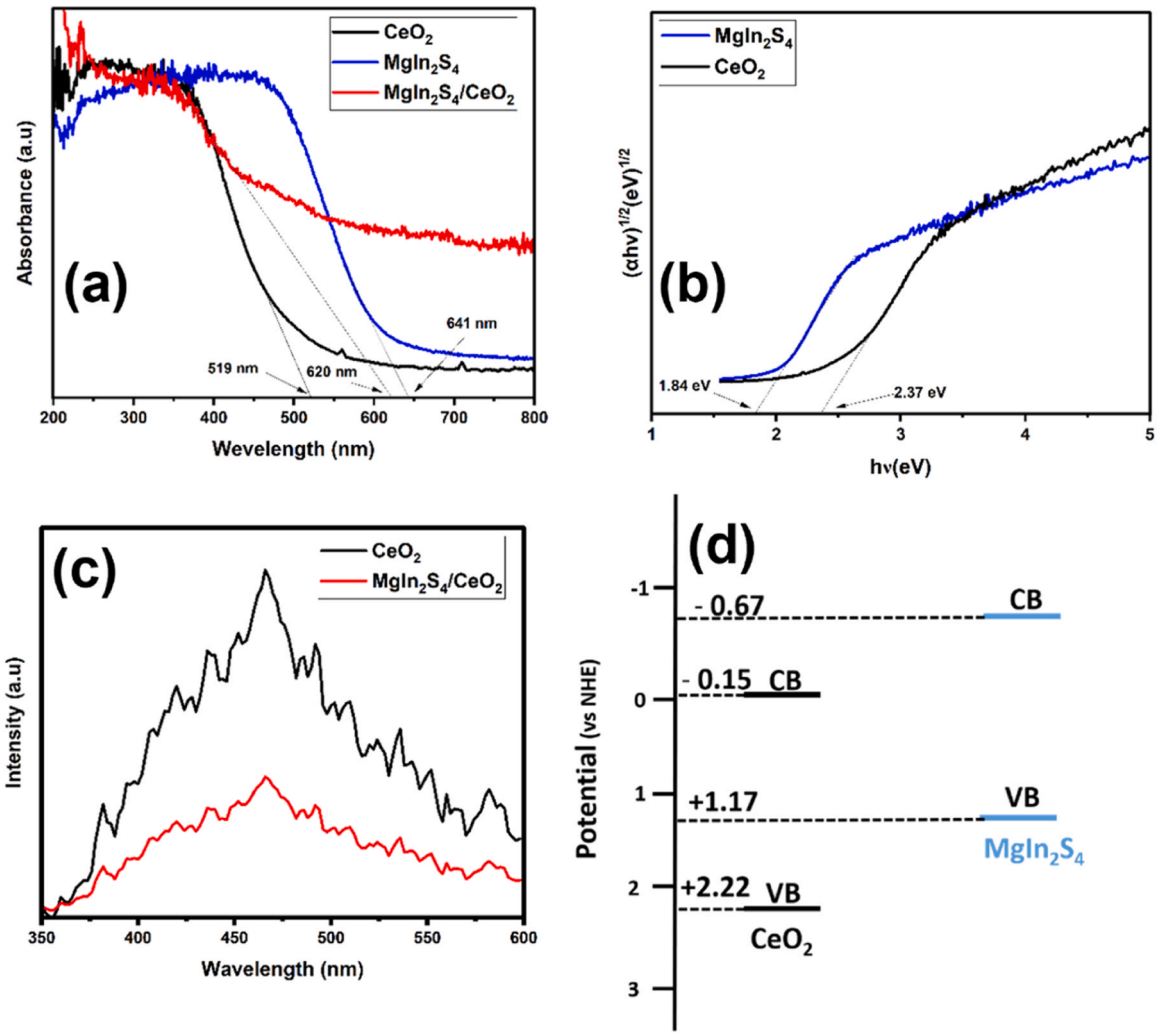


**Fig. 3.** (a) UV-Vis DRS spectra of $CeO_2$, $MgIn_2S_4$ and $MgIn_2S_4/CeO_2$ (b) Tauc plot of $CeO_2$ and $MgIn_2S_4$ (c) Photoluminescence spectra of $CeO_2$ and $MgIn_2S_4$/ $CeO_2$ (d) Band alignment of $CeO_2$ and $MgIn_2S_4$.

due to its low radiative recombination activity. On the other hand, the PL spectrum of the $MgIn_2S_4/CeO_2$ composite shows a noticeable reduction in the peak intensity, which indicates the suppressed recombination rate of photoexcited electron-hole pairs. Therefore, incorporating $MgIn_2S_4$ into $CeO_2$ enhances the overall charge dynamics, and more photogenerated electrons and holes will be allowed to participate in the reduction and oxidation reactions during photocatalysis.

### 3.2.1. *Calculation of conduction and valence bands*

Using Eqs. 2 and 3, the valence (VB) and conduction band (CB) energies of the photocatalyst were calculated.

$$E_c = X - E_o - 0.5E_g \quad (2)$$

$$E_c = E_v - E_g \quad (3)$$

$E_c$ is the conduction band, $E_o$ is free electrons energy on the hydrogen scale (equals to 4.5 eV), $E_g$ is band gap, X is the Mulliken scale of electronegativity (Geometric mean of absolute electronegativity of individual element), and $E_v$ is the valence band.

The Mulliken electronegativity scale was calculated as 4.75 for $MgIn_2S_4$ and 5.53 for $CeO_2$. Hence, as illustrated in Fig. 3d, the calculated $E_c$ and $E_v$ of $CeO_2$ are −0.15 eV and 2.22 eV, while for $MgIn_2S_4$ are −0.67 eV and 1.17 eV, respectively. It is evident that the $E_c$ and $E_v$ edges of $MgIn_2S_4$ and $CeO_2$ are relatively far apart. This band alignment drives efficient charge separation, which helps to retain the high reducing ability of electrons in $MgIn_2S_4$ and the high oxidizing ability of holes in $CeO_2$.

### 3.3. *Photoelectrochemical properties*

The Nyquist plot from the electrochemical impedance spectroscopy was used to determine the photocatalysts' charge transfer resistance ($R_{ct}$). The $R_{ct}$ values obtained from the semi-circles for $CeO_2$, $MgIn_2S_4$, and $MgIn_2S_4/CeO_2$ (Fig. 4a) were found to be approximately 357 Ω, 220 Ω, and 82 Ω, respectively. The $MgIn_2S_4/CeO_2$ composite shows a significantly reduced $R_{ct}$ value, suggesting an enhanced charge transfer efficiency at the heterojunction interface.

The photocurrent measurements under light illumination further validate the superior photocatalytic properties of the $MgIn_2S_4/CeO_2$ composite. As observed (Fig. 4b), $MgIn_2S_4/CeO_2$ possesses the highest photocurrent density of 0.084 mA/cm$^{2,}$ which is 1.47 times greater than that of $MgIn_2S_4$ (0.057 mA/cm2) and 2.27 times greater than that of $CeO_2$ (0.037 mA/cm$^2$). This further buttresses the suppression of the recombination rate of photogenerated electrons and holes.

The flat band potential ($E_{fb}$) of $CeO_2$ and $MgIn_2S_4$ was determined using the Mott-Schottky analysis. Moreover, the positive slopes of the plots of $CeO_2$ (Fig. 4c) and $MgIn_2S_4$ (Fig. 4d) confirm that the photocatalysts are n-type semiconductors. The $E_{fb}$ (vs. Ag/AgCl) of CeO2 and $MgIn_2S_4$ were found to be −0.37 V and − 0.93 V, respectively. The photocatalyst's conduction band (Ec) can also be deduced from the $E_{fb}$.

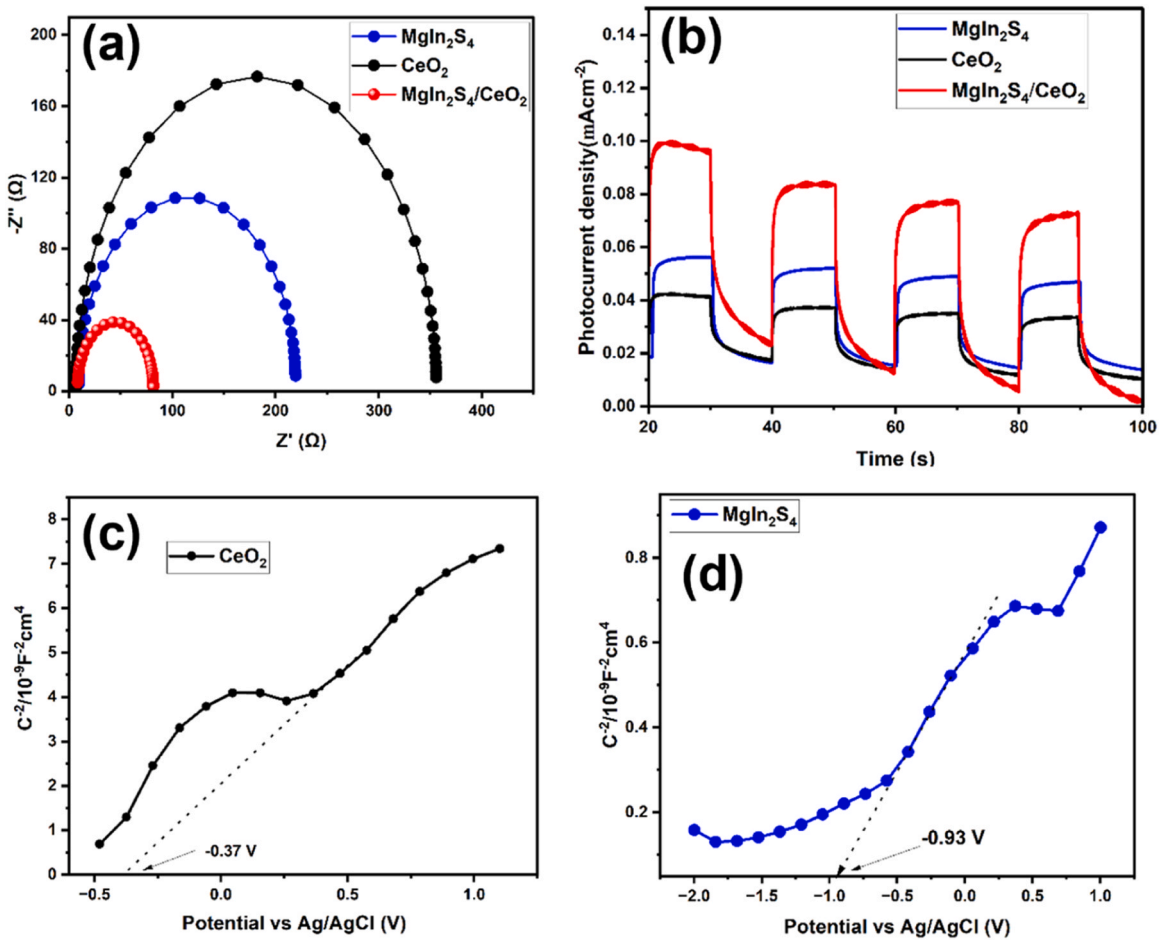


**Fig. 4.** (a) EIS Nyquist plot, (b) Transient photocurrent response of $CeO_2$, $MgIn_2S_4$, and $MgIn_2S_4/CeO_2$. Mott Schottky plot of (c) $CeO_2$, (d) $MgIn_2S_4$.

The $E_{fb}$ (vs. NHE) of $CeO_2$ and $MgIn_2S_4$ is calculated to be – 0.17 eV and -0.73 eV for $CeO_2$ and $MgIn_2S_4$, respectively, by using Eq. 4

$$E_{NHE} = E_{Ag/AgCl} + 0.194 \quad (4)$$

For an n-type semiconductor, Ec is said to be more negative than Efb, with values 0.1–0.2 eV. Therefore, $E_f$ further confirms the calculated $E_c$ of −0.15 eV and −0.67 eV for $CeO_2$ and $MgIn_2S_4$, respectively.

### 3.4. Photocatalytic activities

#### 3.4.1. Photooxidation of tetracycline

The photocatalytic efficiency of $CeO_2$, $MgIn_2S_4$, and $MgIn_2S_4/CeO_2$ were investigated under visible light using tetracycline (TC). As illustrated in Fig. 5a, prior to light irradiation, when 10 mg/L of TC was subjected to photooxidation, no noticeable change in the concentration was observed for $CeO_2$ and $MgIn_2S_4$. However, about a 14 % reduction in TC concentration was observed when the $MgIn_2S_4/CeO_2$ composite was used. This could be attributed to the increase in surface area, leading to more active sites in the $MgIn_2S_4/CeO_2$ composite from the electronic interaction of the pristine photocatalysts. Furthermore, upon light irradiation, 40 %, 52 %, and 86 % degradation efficiency were calculated for $CeO_2$, $MgIn_2S_4$, and $MgIn_2S_4/CeO_2$ after 120 min. Pristine $CeO_2$ and $MgIn_2S_4$ exhibited lower degradation efficiency due to fast rate charge carrier recombination, while $MgIn_2S_4/CeO_2$ demonstrated enhanced photocatalytic degradation due to improved charge separation properties and utilization of the visible light spectrum. The data were analyzed using the pseudo-first-order kinetics, as expressed by Eq. 5. The kinetic plot (Fig. 5b) revealed that the $MgIn_2S_4/CeO_2$ composite exhibited the highest k value (0.0270 min-1), indicating faster degradation rates compared to pristine $CeO_2$ (0.0083 $min^{-1}$) and $MgIn_2S_4$ (0.0073 $min^{-1}$).

$$\ln C_t/C_o = \quad -kt \quad (5)$$

$C_t$ and $C_o$ are tetracycline's final and initial concentrations, and t is the time.

Also, the influence of the pH of the solution on the degradation of TC was investigated at pH 3, 5.2, 7, and 10 (Fig. 2c), and the degradation efficiencies were calculated to be 51 %, 79 %, 86 %, and 36 %, respectively. At near-neutral and neutral pH (5.2 & 7), $MgIn_2S_4/CeO_2$ exhibited better degradation efficiency. In comparison, the degradation efficiency was lower in acidic conditions, likely due to the protonation of tetracycline, thus reducing its interaction with the photocatalyst surface [42]. Similarly, the degradation efficiency was the lowest at alkaline conditions, and this can be due to the formation of hydroxyl complexes with TC that may hinder the interaction with the photocatalyst [43]. Thus, pH 7 was used as the optimal pH for the degradation of TC. Hence, the results suggest that $MgIn_2S_4/CeO_2$ performs better under a near-neutral environment, making it suitable for practical applicability in water treatment.

Moreover, the effect of the catalyst dosage on TC degradation was also investigated at mass dosages of 10, 20, 30, 40, and 50 mg (Fig. 2d), and the degradation efficiency was calculated to be 44 %, 63 %, 84 %, 86 %, and 86 %, respectively. At low dosages of 10 mg and 30 mg, the degradation efficiency was observed to be relatively low, which can be due to insufficient availability of active sites. A 2 % increase in degradation efficiency was observed when the catalyst dosage was increased to 40 mg, and afterward, no change was observed at a higher dosage of 50 mg; this could be due to excess catalyst loading that can lead to light

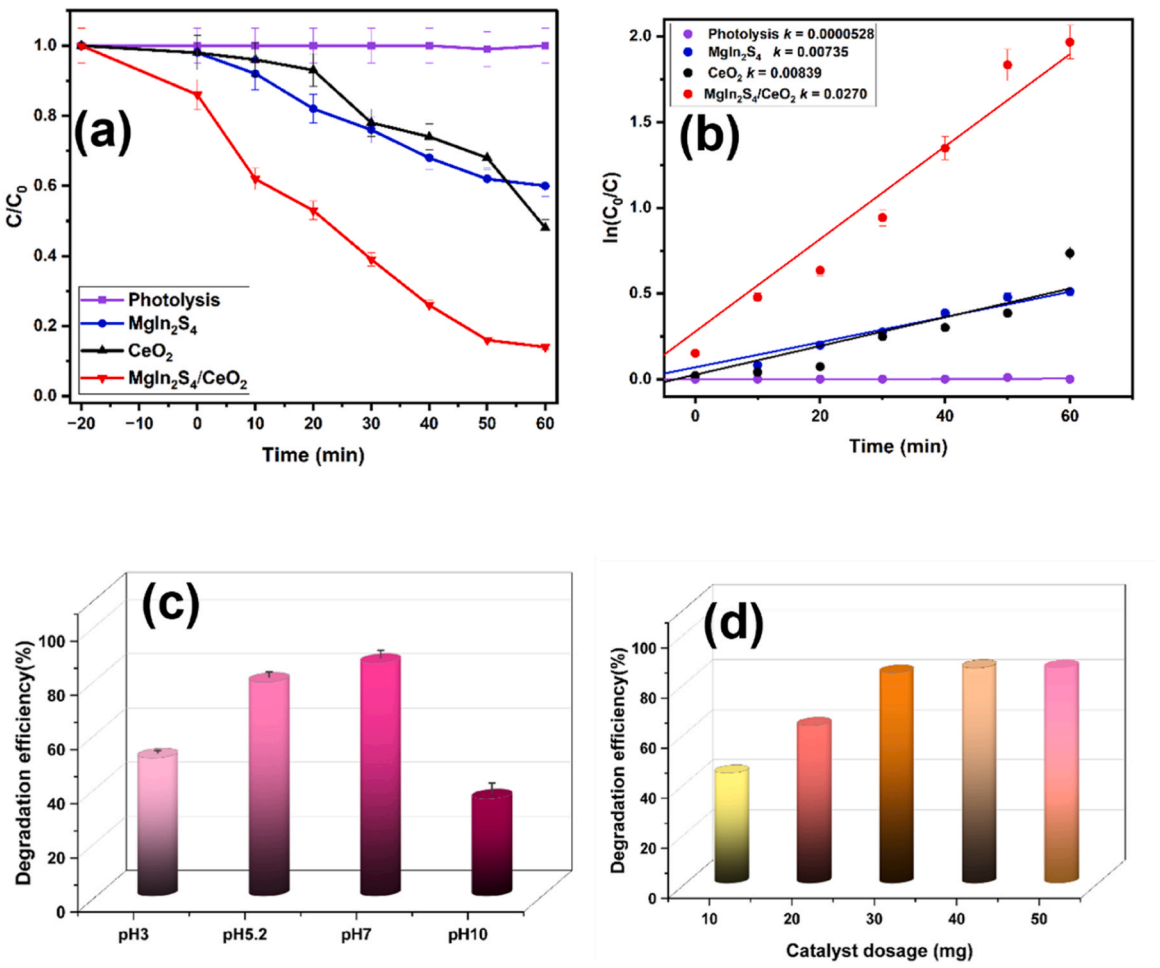


**Fig. 5.** (a)Effect of photocatalyst, (b) Kinetic studies, (c) Effect of pH, (d) Effect of catalyst dosage, in the photooxidation of tetracycline.

scattering. As a result, 40 mg was used as the optimal catalyst dosage.

Furthermore, the total organic carbon (TOC) measurements were conducted to assess the mineralization efficiency of $MgIn_2S_4/CeO_2$. The plot in Figure S1 shows a significant reduction after 120 min with a TOC efficiency of 48 %, indicating that the $MgIn_2S_4/CeO_2$ heterojunction degrades TC and effectively mineralizes it into intermediates and smaller molecules.

The long-term stability of the photocatalyst was determined by evaluating its reusability. Successive photocatalytic reactions were conducted for five cycles under the same reaction conditions (Figure S2). The degradation efficiency of TC was observed to decrease slightly after the 4th cycle treatment from 86 % to 84 %. This minor reduction suggests good stability of $MgIn_2S_4/CeO_2$. Notably, the photoactivity of $MgIn_2S_4/CeO_2$ compared favourably with numerous $CeO_2$-based heterojunction photocatalysts (Table 2).

### 3.4.2. *Photoreduction of Cr(VI)*

In addition to the photooxidation reaction, the photoreduction of Cr (VI) experiment was conducted to evaluate the performance of $MgIn_2S_4/CeO_2$ composite under visible light irradiation. Similarly, as illustrated in Fig. 6a, negligible changes in the Cr(VI) concentration were observed for $MgIn_2S_4$ and $CeO_2$ when left in the dark before light irradiation. In contrast, minimal Cr(VI) absorption, yielding about 21 % degradation efficiency, was observed for $MgIn_2S_4/CeO_2$ before light irradiation. Aside from that, the degradation efficiency of $MgIn_2S_4$, $CeO_2$, and $MgIn_2S_4/CeO_2$ in the photoreduction of Cr(VI) is 70 %, 28 %, and 96 %, respectively, and the absence of light irradiation has no notable change in the concentration. Subsequently, the data obtained were fitted to the pseudo-first order model in Eq. 5. The reaction rate constant (k) for $MgIn_2S_4/CeO_2$ composite was calculated as 0.0391 $min^{-1}$ which is 2.3 and 8.6 times greater than the k values obtained for $MgIn_2S_4$ (0.0167 $min^{-1}$ and $CeO_2$ (0.0045 $min^{-1}$), respectively (Fig. 6b).

Therefore, $MgIn_2S_4/CeO_2$ is as efficient for photooxidation and photoreduction, owing to the S-scheme heterojunction where the photogenerated hole and electron with the highest oxidation and reduction potential are preserved to remove pollutants in water.

**Table 2**
Comparison $CeO_2$-based photocatalysts.

| Photocatalysts | Light Source | Catalyst Dosage | CIP parameters | Degradation rate | Rate constant | Ref |
|---|---|---|---|---|---|---|
| $CeO_2/ZnO$ | 200 W Hg-Xe lamp | 50 mg | 100 mL, 15 mg/L | 85 % | 0.0130 $min^{-1}$ | [44] |
| $Bi_2WO_6/CeO_2$ | 300 W xenon lamp | 20 mg | 50 mL, 30 mg/L | 86.6 % | 0.0246 $min^{-1}$ | [45] |
| $CeO_2$-Ag/AgBr | 300 W, Xe lamp | 50 mg | 50 mL, 10 mg/L | 93.05 % | 0.02011 $min^{-1}$ | [46] |
| $CeO_2$/CdS/RGO | 800 W, Xe | 20 mg | 40 mL, 40 mg/L | 90 % | 0.015 $min^{-1}$ | [47] |
| $Cd0.5Zn_{0.5}S/CeO_2$ | 100 W, Xe | 30 mg/L | 50 mL, 5 mg/L | 86 % | 0.0454 $min^{-1}$ | [13] |
| $MgIn_2S_4/CeO_2$ | 100 W, Xe | 40 mg/L | 50 mL, 5 mg/L | 86 % | 0.0454 $min^{-1}$ | |

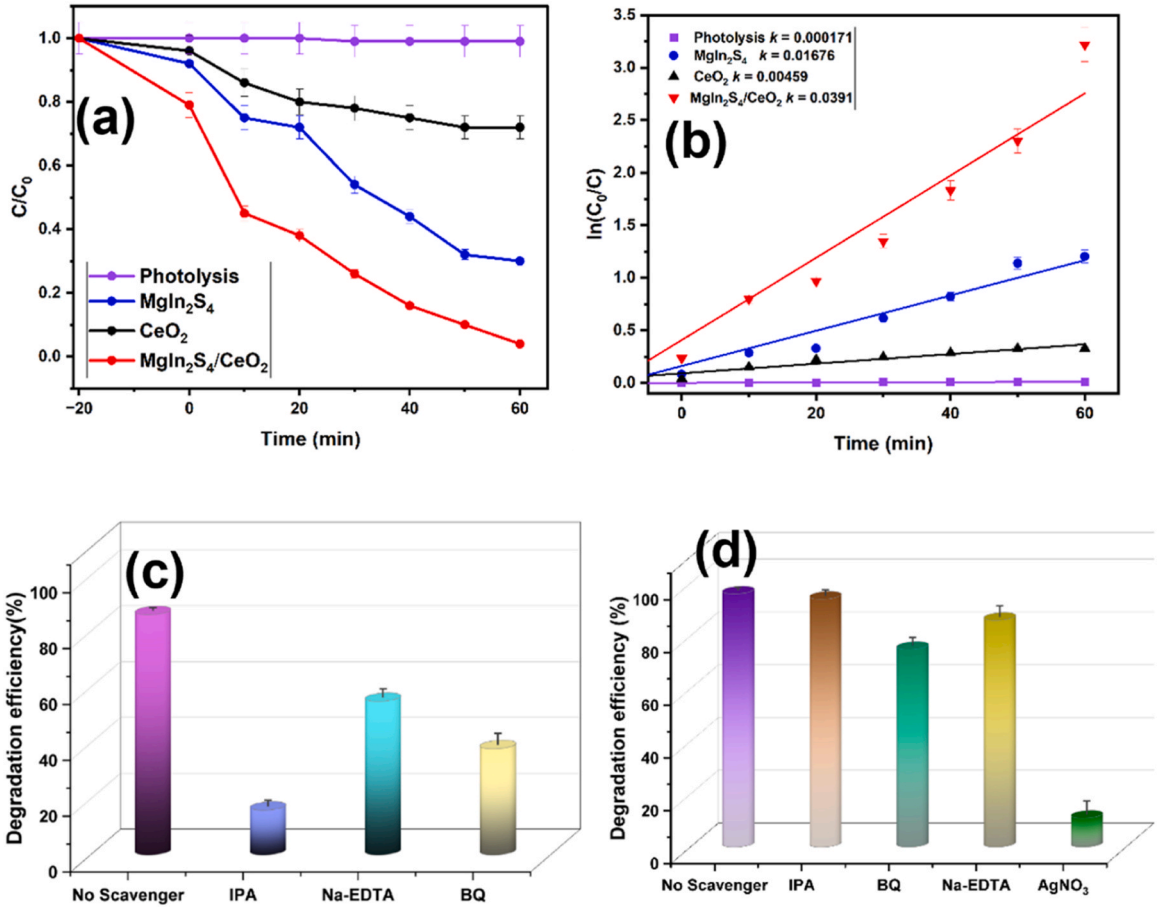


**Fig. 6.** (a)Effect of photocatalyst, (b) Kinetic studies in the photoreduction of Cr(VI). Radical testing experiment of $MgIn_2S_4/CeO_2$ in (c) the photooxidation of tetracycline, (d) the photoreduction of Cr(VI).

### 3.4.3. *Radical testing*

The radical testing experiment was conducted to identify the reactive species responsible for the oxidation and reduction reactions of tetracycline and Cr(VI), respectively. For the photooxidation reaction of tetracycline over $MgIn_2S_4/CeO_2$ photocatalyst, the scavenger studies (Fig. 6c) reveal that upon the addition of Na-EDTA ($h^+$ scavenger) and benzoquinone ($O_2\bullet^-$ scavenger), the degradation efficiency reduced from 86 % to 55 % and 38 %, respectively. And when isopropanol (•OH scavenger) was added to the TC solution, the degradation efficiency was reduced to 16 %. These indicate that hydroxyl radical is the major species responsible for the degradation of tetracycline, with secondary contributions from the photogenerated holes and superoxide anion radicals. Conversely, for the photoreduction of Cr(VI) over $MgIn_2S_4/CeO_2$ photocatalyst, the radical testing experiment (Fig. 6d) shows that upon the addition of isopropanol (•OH scavenger), benzoquinone ($O_2\bullet^-$ scavenger), and Na-EDTA ($h^+$ scavenger), the degradation efficiency reduced from 96 % to 94 %, 75 %, and 86 %, respectively, showing their minor contributions in the photoreduction reaction. As expected, when $AgNO_3$ (e-scavenger) was added, the degradation efficiency decreased from 96 % to 11 %, indicating that photogenerated electrons play an essential role in the reduction of Cr(VI).

### 3.4.4. *Degradation product and pathway*

Typically, the degradation of tetracycline proceeds through oxidation, hydrolysis, and photolytic reactions influenced by the reactive oxygen species. The UPLC-MS spectra (Figure S3) were used to predict the intermediates and products of the degradation of tetracycline using $MgIn_2S_4/CeO_2$ heterojunction. The detection of an ion at approximately *m/z* 445 reveals tetracycline. The initial step involves the reduction of the carbonyl group of the amide to form a hydroxyl group (formamide), which renders the compound *m/z* 446 unstable, and further breakdown to the compound *m/z* 427 due to loss of a water molecule. Further oxidation process involving the D-ring led to a deamination process where the dimethylamine and amine groups were removed, and the hydroxyl group was replaced by a methyl group (*m/z* 290). Furthermore, the cleavage of the C-ring led to the formation of the compound *m/z* 144, and the opening of the ring gave rise to the by-product, the alkanol group (*m/z* 103). The toxicity of the byproduct in comparison to tetracycline was investigated using obtained is less toxic when toxicity estimation software tool (T.E.S.T), and the $LC_{50}$ value for tetracycline is 0.25 mg/L while for the proposed byproduct is 65.75 mg/L, and based on the toxicity rule for fathead minnow, $LC_{50}$ values between 0 and 1 is considered very toxic while 10–500 mg/L can be considered harmful. Thus, a decrease in toxicity of tetracycline was observed upon photooxidation using $MgIn_2S_4/CeO_2$ heterojunction (Scheme 1).

## 4. Mechanism of heterojunction formation and photocatalytic reaction

Based on the results and observations, particularly from band energies calculations and Mott Schottky analysis, the most appropriate type of band alignment observed from the combination of $CeO_2$ and $MgIn_2S_4$ is the type II heterojunction, where the CB of one photocatalyst is more negative than the CB of the other and the respective CB is less positive that the VB of the other, thus forming a staggered structure. Conversely, the results from the radical testing experiment oppose the charge transfer dynamics associated with the type II heterojunction because the oxidation potential of the photogenerated hole in the VB is

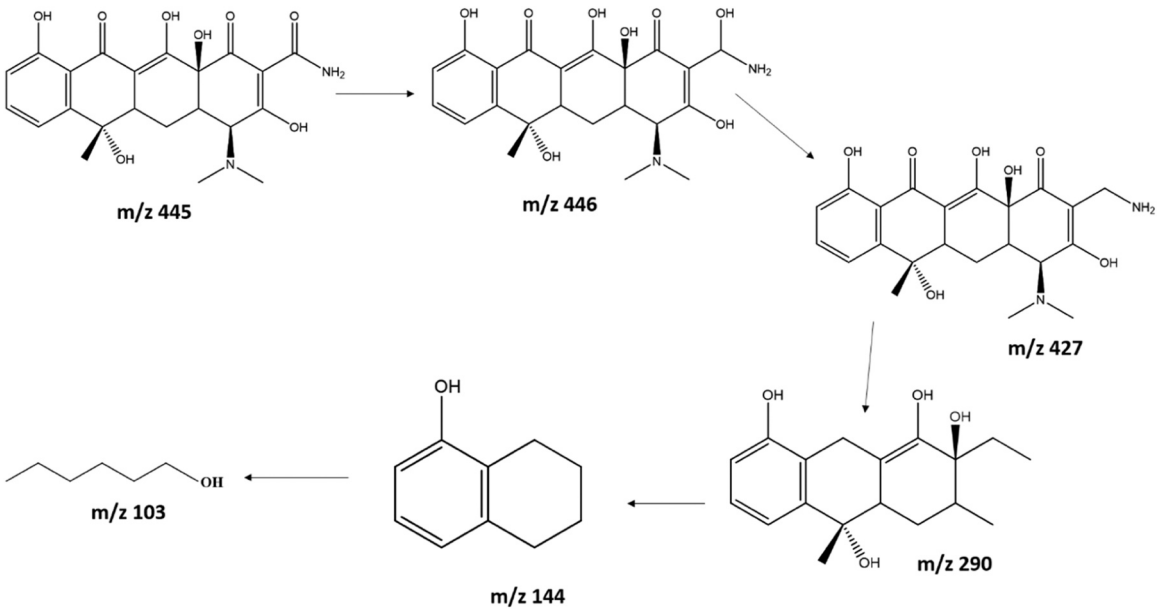


**Scheme 1.** Proposed degradation pathway and products of tetracycline using $MgIn_2S_4/CeO_2$ photocatalyst.

insufficient to oxidize water to generate hydroxyl radicals for the photooxidation process. ($\bullet OH/H_2O = +2.26$ V), although the photogenerated electron can directly reduce Cr (VI). And, in relation to the XPS spectra, the proposed type of heterojunction formed from the combination of $CeO_2$ and $MgIn_2S_4$ is the S-scheme heterojunction where the electrons in the CB of $MgIn_2S_4$ and the holes in the VB of $CeO_2$ with the highest potentials were used for the photooxidation and photoreduction reactions. Typically, as illustrated in Scheme 2, when $CeO_2$ and $MgIn_2S_4$ combine, in order for a Fermi level equilibrium to be reached, electrons in the CB of $MgIn_2S_4$ (electron-rich) will migrate to the CB of $CeO_2$ (electron-deficient). This charge transfer will increase electron density around $CeO_2$ and create an internal electric field in the direction from $MgIn_2S_4$ to $CeO_2$. Then, upon light irradiation, the electron density around $CeO_2$ will cause a downward bending in the CB and an upward banding in the CB of c. As a result, the photogenerated electrons of $CeO_2$ will recombine with the photogenerated hole of $MgIn_2S_4$, thus creating an efficient charge separation that allows for the preservation of the photogenerated hole of $CeO_2$ and photogenerated electrons of $MgIn_2S_4$ for oxidation and reduction purposes, respectively. Unlike the type II heterojunction, the S- scheme eliminates weak redox charge carriers.

In summary, the proposed photocatalytic pathway is illustrated in Eqs. 6–11

$$MgIn_2S_4 + hv \rightarrow MgIn_2S_4\ (e^-_{CB} + h^+_{VB}) \quad (6)$$

$$CeO_2 + hv \rightarrow CeO_2\ (e^-_{CB} + h^+_{VB}) \quad (7)$$

$$e^-_{CB}\ (CeO_2) + h^+_{VB}\ (MgIn_2S_4) \rightarrow \text{Recombination} \quad (8)$$

$$h^+_{VB}\ (CeO_2) + H_2O \rightarrow \bullet OH + H^+ \quad (9)$$

$$e^-_{CB}\ (MgIn_2S_4) + O_2 \rightarrow O_2\bullet^- \quad (10)$$

$$h^+_{VB}\ (CeO_2)/\ \bullet OH/\ O_2\bullet^- + TC \rightarrow \text{smaller molecules} \rightarrow \rightarrow CO_2 + H_2O \quad (11)$$

$$e^-_{CB}\ (MgIn_2S_4) + Cr(VI) \rightarrow Cr \quad (III)$$

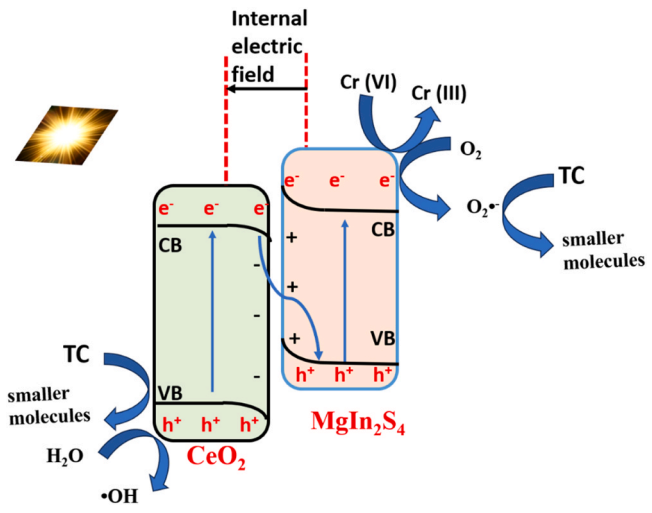


**Scheme 2.** Proposed degradation mechanism involved in the photocatalytic reaction using $MgIn_2S_4/CeO_2$ S-scheme heterojunction.

## 5. Conclusion

The study successfully demonstrates the synthesis and characterization of $MgIn_2S_4/CeO_2$ of heterojunction with significantly enhanced photocatalytic activity under visible light irradiation. Central to this enhancement is forming the S-scheme heterojunction, which optimizes electron-hole pair dynamics by facilitating charge recombination of low-energy carriers while preserving the photogenerated carriers with the highest redox potentials. This unique electronic configuration ensures efficient charge separation and promotes superior oxidation and reduction processes, the key to the degradation of tetracycline and the reduction of Cr(VI). The hierarchical porous structure of $MgIn_2S_4$, combined with the uniformly distributed $CeO_2$ nanoparticles, further enhances light absorption and provides abundant active sites for photocatalytic reactions. These synergistic structural and electronic features emphasize the potential of $MgIn_2S_4/CeO_2$ as a versatile and efficient photocatalyst for environmental applications, particularly in wastewater treatment.

## CRediT authorship contribution statement

**Akintayo Damilola Caleb:** Writing – review & editing, Writing – original draft, Investigation, Conceptualization. **Yusuf Tunde Lewis:** Writing – review & editing, Writing – original draft, Investigation,

Conceptualization. **Mabuba Nonhlangabezo:** Writing – review & editing, Conceptualization.

## Declaration of Competing Interest

The authors declare that they have no known competing financial interests or personal relationships that could have appeared to influence the work reported in this paper.

## Appendix A. Supporting information

Supplementary data associated with this article can be found in the online version at doi:10.1016/j.colsurfa.2025.137215.

## Data availability

Data will be made available on request.

## References


[1] F.N. Chaudhry, M. Malik, Factors affecting water pollution: a review, J. Ecosyst. Ecogr. 7 (2017) 225–231, https://doi.org/10.4172/2157-7625.100022.

[2] S.H. Hassan Al-Taai, Water pollution Its causes and effects, IOP Conference Series: Earth and Environmental Science, 790 (2021) 012026.10.1088/1755-1315/790/1/012026DOI: 10.1088/1755-1315/790/1/012026.

[3] N. Quinete, R.A. Hauser-Davis, Drinking water pollutants may affect the immune system: concerns regarding COVID-19 health effects, Environ. Sci. Pollut. Res. 28 (2021) 1235–1246, https://doi.org/10.1007/s11356-020-11487-4.

[4] S. Ren, S. Wang, Y. Liu, Y. Wang, F. Gao, Y. Dai, A review on current pollution and removal methods of tetracycline in soil, Sep. Sci. Technol. 58 (2023) 2578–2602, https://doi.org/10.1080/01496395.2023.2259079.

[5] O.C. Olatunde, T.L. Yusuf, N. Mabuba, D.C. Onwudiwe, S. Makgato, Interfacial electron redistribution in 2D/3D MoS2/CuBi2O4 p-n heterojunction for visible light assisted reduction of Cr(VI) and oxidation of antibiotics, J. Water Process Eng. 59 (2024) 105074, https://doi.org/10.1016/j.jwpe.2024.105074.

[6] Y. Amangelsin, Y. Semenova, M. Dadar, M. Aljofan, G. Bjorklund, The impact of tetracycline pollution on the aquatic environment and removal strategies, Antibiotics 12 (2023) 440, https://doi.org/10.3390/antibiotics12030440.

[7] J. Antos, M. Piosik, D. Ginter-Kramarczyk, J. Zembrzuska, I. Kruszelnicka, Tetracyclines contamination in European aquatic environments: A comprehensive review of occurrence, fate, and removal techniques, Chemosphere 353 (2024) 141519, https://doi.org/10.1016/j.chemosphere.2024.141519.

[8] P. Sharma, S.P. Singh, S.K. Parakh, Y.W. Tong, Health hazards of hexavalent chromium (Cr (VI)) and its microbial reduction, Bioengineered 13 (2022) 4923–4938, https://doi.org/10.1080/21655979.2022.2037273.

[9] M.-N. Georgaki, M. Charalambous, Toxic chromium in water and the effects on the human body: a systematic review, J. Water Health 21 (2023) 205–223, https://doi.org/10.2166/wh.2022.214.

[10] H. Sun, J. Brocato, M. Costa, Oral chromium exposure and toxicity, Curr. Environ. Health Rep. 2 (2015) 295–303, https://doi.org/10.1007/s40572-015-0054-z.

[11] R. Ameta, M.S. Solanki, S. Benjamin, S.C. Ameta, Chapter 6 - Photocatalysis, in: S. C. Ameta, R. Ameta (Eds.), Advanced Oxidation Processes for Waste Water Treatment, Academic Press, 2018, pp. 135–175, https://doi.org/10.1016/B978-0-12-810499-6.00006-1.

[12] O.C. Olatunde, L. Sawunyama, T.L. Yusuf, D.C. Onwudiwe, Visible light driven CuBi2O4 heterostructures and their enhanced photocatalytic activity for pollutant degradation: a review, J. Water Process Eng. 66 (2024) 105890, https://doi.org/10.1016/j.jwpe.2024.105890.

[13] T.L. Yusuf, O.C. Olalekan, D. Masekela, N. Mabuba, D. Onwudiwe, S. Makgato, Rational design of S-Scheme Cd0.5Zn0.5S/CeO2 heterojunction for enhanced photooxidation of antibiotics and photoreduction of Cr(VI), Ceram. Int. (2024), https://doi.org/10.1016/j.ceramint.2024.08.397.

[14] M.A. Al-Nuaim, A.A. Alwasiti, Z.Y. Shnain, The photocatalytic process in the treatment of polluted water, Chem. Pap. 77 (2023) 677–701, https://doi.org/10.1007/s11696-022-02468-7.

[15] T.L. Yusuf, B.O. Orimolade, D. Masekela, B. Mamba, N. Mabuba, The application of photoelectrocatalysis in the degradation of rhodamine B in aqueous solutions: a review, RSC Adv. 12 (2022) 26176–26191, https://doi.org/10.1039/d2ra04236c.

[16] D. Masekela, N.C. Hintsho-Mbita, S. Sam, T.L. Yusuf, N. Mabuba, Application of BaTiO3-based catalysts for piezocatalytic, photocatalytic and piezo-photocatalytic degradation of organic pollutants and bacterial disinfection in wastewater: a comprehensive review, Arab. J. Chem. 16 (2023) 104473, https://doi.org/10.1016/j.arabjc.2022.104473.

[17] J. Iyyappan, B. Gaddala, R. Gnanasekaran, M. Gopinath, D. Yuvaraj, V. Kumar, Critical review on wastewater treatment using photo catalytic advanced oxidation process: role of photocatalytic materials, reactor design and kinetics, Case Stud. Chem. Environ. Eng. 9 (2024) 100599, https://doi.org/10.1016/j.cscee.2023.100599.

[18] H. Liu, C. Wang, G. Wang, Photocatalytic advanced oxidation processes for water treatment: recent advances and perspective, Chem. Asian J. 15 (2020) 3239–3253, https://doi.org/10.1002/asia.202000895.

[19] K. Mishra, N. Devi, S.S. Siwal, V.K. Gupta, V.K. Thakur, Hybrid semiconductor photocatalyst nanomaterials for energy and environmental applications: fundamentals, designing, and prospects, Adv. Sustain. Syst. 7 (2023) 2300095, https://doi.org/10.1002/adsu.202300095.

[20] X. Li, Y. Chen, Y. Tao, L. Shen, Z. Xu, Z. Bian, H. Li, Challenges of photocatalysis and their coping strategies, Chem. Catal. 2 (2022) 1315–1345, https://doi.org/10.1016/j.checat.2022.04.007.

[21] S. Manna, N. Remya, N. Singhal, Advancements in S-scheme photocatalytic material for wastewater treatment, J. Environ. Chem. Eng. 11 (2023) 109838, https://doi.org/10.1016/j.jece.2023.109838.

[22] L. Zhang, J. Zhang, H. Yu, J. Yu, Emerging S-scheme photocatalyst, Adv. Mater. 34 (2022) 2107668, https://doi.org/10.1002/adma.202107668.

[23] Q. Xu, L. Zhang, B. Cheng, J. Fan, J. Yu, S-scheme heterojunction photocatalyst, Chem 6 (2020) 1543–1559, https://doi.org/10.1016/j.chempr.2020.06.010.

[24] Q. Xu, S. Wageh, A.A. Al-Ghamdi, X. Li, Design principle of S-scheme heterojunction photocatalyst, J. Mater. Sci. Technol. 124 (2022) 171–173, https://doi.org/10.1016/j.jmst.2022.02.016.

[25] Z.-J. Chen, H. Guo, H.-Y. Liu, C.-G. Niu, D.-W. Huang, Y.-Y. Yang, C. Liang, L. Li, J.-C. Li, Construction of dual S-scheme Ag2CO3/Bi4O5I2/g-C3N4 heterostructure photocatalyst with enhanced visible-light photocatalytic degradation for tetracycline, Chem. Eng. J. 438 (2022) 135471, https://doi.org/10.1016/j.cej.2022.135471.

[26] S. Wu, X. Yu, J. Zhang, Y. Zhang, Y. Zhu, M. Zhu, Construction of BiOCl/CuBi2O4 S-scheme heterojunction with oxygen vacancy for enhanced photocatalytic diclofenac degradation and nitric oxide removal, Chem. Eng. J. 411 (2021) 128555, https://doi.org/10.1016/j.cej.2021.128555.

[27] A. Kane, L. Chafiq, S. Dalhatou, P. Bonnet, M. Nasr, N. Gaillard, J.M.D. Dikdim, G. Monier, A.A. Assadi, H. Zeghioud, g-C3N4/TiO2 S-scheme heterojunction photocatalyst with enhanced photocatalytic Carbamazepine degradation and mineralization, J. Photochem. Photobiol. A Chem. 430 (2022) 113971, https://doi.org/10.1016/j.jphotochem.2022.113971.

[28] A. Bahadoran, S. Ramakrishna, S. Masudy-Panah, J.R. De Lile, B. Sadeghi, J. Li, J. Gu, Q. Liu, Novel S-scheme WO3/CeO2 heterojunction with enhanced photocatalytic degradation of sulfamerazine under visible light irradiation, Appl. Surf. Sci. 568 (2021) 150957, https://doi.org/10.1016/j.apsusc.2021.150957.

[29] J. Luo, P. Lin, P. Zheng, X. Zhou, X. Ning, L. Zhan, Z. Wu, X. Liu, X. Zhou, In suit constructing S-scheme FeOOH/MgIn2S4 heterojunction with boosted interfacial charge separation and redox activity for efficiently eliminating antibiotic pollutant, Chemosphere 298 (2022) 134297, https://doi.org/10.1016/j.chemosphere.2022.134297.

[30] A.A. Fauzi, A.A. Jalil, N.S. Hassan, F.F.A. Aziz, M.S. Azami, I. Hussain, R. Saravanan, D.V.N. Vo, A critical review on relationship of CeO2-based photocatalyst towards mechanistic degradation of organic pollutant, Chemosphere 286 (2022) 131651, https://doi.org/10.1016/j.chemosphere.2021.131651.

[31] K.A. Hoque, S.A. Sathi, F. Akter, T. Akter, T. Ahmed, W. Ullah, K. Arafin, M. S. Rahaman, H.M. Shahadat, A.B. Imran, Recent advances on photocatalytic CO2 reduction using CeO2-based photocatalysts: a review, J. Environ. Chem. Eng. (2024) 113487, https://doi.org/10.1016/j.jece.2024.113487.

[32] O.C. Olatunde, I. Waziri, D.C. Onwudiwe, T.L. Yusuf, Design of S-scheme CuInS2/CeO2 heterojunction for enhanced photocatalytic degradation of pharmaceuticals in wastewater, Langmuir 41 (2025) 2480–2491, https://doi.org/10.1021/acs.langmuir.4c04175.

[33] K.D. Jayeola, D.S. Sipuka, T.I. Sebokolodi, O.V. Nkwachukwu, C. Muzenda, B. A. Koiki, J.O. Babalola, M. Zhou, O.A. Arotiba, An S-Scheme CeO2/Bi2O2S heterojunction photoanode for the photoelectrocatalytic degradation of sulfamethoxazole in synthetic and real wastewater, Electrochim. Acta (2024) 145160, https://doi.org/10.1016/j.electacta.2024.145160.

[34] Z.-w Zhang, R.-t Guo, J. Tang, Y.-f Miao, J.-w Gu, W.-g Pan, Fabrication of Bi-BiOCl/MgIn2S4 heterostructure with step-scheme mechanism for carbon dioxide photoreduction into methane, J. CO2 Util. 45 (2021) 101453, https://doi.org/10.1016/j.jcou.2021.101453.

[35] W. Chen, Y.-X. Hua, Y. Wang, T. Huang, T.-Y. Liu, X.-H. Liu, Two-dimensional mesoporous g-C3N4 nanosheet-supported MgIn2S4 nanoplates as visible-light-active heterostructures for enhanced photocatalytic activity, J. Catal. 349 (2017) 8–18, https://doi.org/10.1016/j.jcat.2017.01.005.

[36] T.L. Yusuf, S.A. Ogundare, F. Opoku, O.A. Arotiba, N. Mabuba, Theoretical and experimental insight into the construction of FTO/NiSe2/BiVO4 photoanode towards an efficient charge separation for the degradation of pharmaceuticals in water, J. Environ. Chem. Eng. 11 (2023) 110711, https://doi.org/10.1016/j.jece.2023.110711.

[37] Q. Liu, S. Dong, H. Jin, S. Ke, L. Luo, T. Huang, Preparation of MgIn2S4/g-C3N4 for enhanced ranitidine photocatalytic degradation activity via Z-scheme electron transfer, J. Environ. Chem. Eng. 11 (2023) 111568, https://doi.org/10.1016/j.jece.2023.111568.

[38] A. Das, N. S.K, R.G. Nair, Influence of surface morphology on photocatalytic performance of zinc oxide: a review, Nano Struct. Nano-Objects 19 (2019) 100353, https://doi.org/10.1016/j.nanoso.2019.100353.

[39] H. Wang, X. Liu, P. Niu, S. Wang, J. Shi, L. Li, Porous two-dimensional materials for photocatalytic and electrocatalytic applications, Matter 2 (2020) 1377–1413, https://doi.org/10.1016/j.matt.2020.04.002.

[40] K.I. Maslakov, Y.A. Teterin, A.J. Popel, A.Y. Teterin, K.E. Ivanov, S.N. Kalmykov, V. G. Petrov, P.K. Petrov, I. Farnan, XPS study of ion irradiated and unirradiated CeO2

bulk and thin film samples, Appl. Surf. Sci. 448 (2018) 154–162, https://doi.org/10.1016/j.apsusc.2018.04.077.
[41] H.-Y. Liu, C.-G. Niu, H. Guo, C. Liang, D.-W. Huang, L. Zhang, Y.-Y. Yang, L. Li, In suit constructing 2D/1D MgIn2S4/CdS heterojunction system with enhanced photocatalytic activity towards treatment of wastewater and H2 production, J. Colloid Interface Sci. 576 (2020) 264–279, https://doi.org/10.1016/j.jcis.2020.05.025.
[42] J. Chen, X. Xiao, Y. Wang, M. Lu, X. Zeng, Novel AgI/BiOBr/reduced graphene oxide Z-scheme photocatalytic system for efficient degradation of tetracycline, J. Alloy. Compd. 800 (2019) 88–98, https://doi.org/10.1016/j.jallcom.2019.06.004.
[43] K. Divakaran, A. Baishnisha, V. Balakumar, K.N. Perumal, C. Meenakshi, R. S. Kannan, Photocatalytic degradation of tetracycline under visible light using TiO2@sulfur doped carbon nitride nanocomposite synthesized via in-situ method, J. Environ. Chem. Eng. 9 (2021) 105560, https://doi.org/10.1016/j.jece.2021.105560.
[44] L. Wolski, K. Grzelak, M. Muńko, M. Frankowski, T. Grzyb, G. Nowaczyk, Insight into photocatalytic degradation of ciprofloxacin over CeO2/ZnO nanocomposites: unravelling the synergy between the metal oxides and analysis of reaction pathways, Appl. Surf. Sci. 563 (2021) 150338, https://doi.org/10.1016/j.apsusc.2021.150338.
[45] J. Chen, Z. Yan, Y. Ding, G. Wang, Z. Xu, Constructing oxygen defect-rich Bi2WO6/CeO2 S-scheme heterojunction for boosted photocatalytic antibiotic removal, Chem. Eng. Sci. 287 (2024) 119715, https://doi.org/10.1016/j.ces.2024.119715.
[46] X.-J. Wen, C.-G. Niu, L. Zhang, C. Liang, H. Guo, G.-M. Zeng, Photocatalytic degradation of ciprofloxacin by a novel Z-scheme CeO2–Ag/AgBr photocatalyst: influencing factors, possible degradation pathways, and mechanism insight, J. Catal. 358 (2018) 141–154, https://doi.org/10.1016/j.jcat.2017.11.029.
[47] J. Yao, Z. Gao, Q. Meng, G. He, H. Chen, One-step synthesis of reduced graphene oxide based ceric dioxide modified with cadmium sulfide (CeO2/CdS/RGO) heterojunction with enhanced sunlight-driven photocatalytic activity, J. Colloid Interface Sci. 594 (2021) 621–634, https://doi.org/10.1016/j.jcis.2021.03.034.